The Astronomical Journal, 156:289 (15pp), 2018 December https://doi.org/10.3847/1538-3881/aaed46

WFIRST Exoplanet Mass-measurement Method Finds a Planetary Mass of $39 \pm 8 M_{\oplus}$ for OGLE-2012-BLG-0950Lb

A. Bhattacharya[1,2], J.-P. Beaulieu[3,4], D. P. Bennett[1,2], J. Anderson[5], N. Koshimoto[6,7], J. R. Lu[8], V. Batista[3], J. W. Blackman[4], I. A. Bond[9], A. Fukui[10], C. B. Henderson[11], Y. Hirao[2,12], J. B. Marquette[3], P. Mroz[13], C. Ranc[14], and A. Udalski[13]

[1] Code 667, NASA Goddard Space Flight Center, Greenbelt, MD 20771, USA; aparna.bhattacharya@nasa.gov
[2] Department of Astronomy, University of Maryland, College Park, MD 20742, USA
[3] UPMC-CNRS, UMR 7095, Institut d'Astrophysique de Paris, 98 Bis Boulevard Arago, F-75014 Paris, France
[4] School of Physical Sciences, University of Tasmania, Private Bag 37, Hobart, TAS 7001, Australia
[5] Space Telescope Science Institute, 3700 San Martin Drive, Baltimore, MD 21218, USA
[6] Department of Astronomy, Graduate School of Science, The University of Tokyo, 7-3-1 Hongo, Bunkyo-ku, Tokyo 113-0033, Japan
[7] National Astronomical Observatory of Japan, 2-21-1 Osawa, Mitaka, Tokyo 181-8588, Japan
[8] University of California Berkeley, Berkeley, CA, USA
[9] Institute of Natural and Mathematical Sciences, Massey University, Auckland 0745, New Zealand
[10] Okayama Astrophysical Observatory, National Astronomical Observatory of Japan, Asakuchi, 719-0232 Okayama, Japan
[11] NASA Exoplanet Science Institute, IPAC/Caltech, Pasadena, CA 91125, USA
[12] Department of Earth and Space Science, Graduate School of Science, Osaka University, 1-1 Machikaneyama, Toyonaka, Osaka 560-0043, Japan
[13] Warsaw University Observatory, Al. Ujazdowskie 4, 00-478 Warszawa, Poland
[14] Code 660, NASA Goddard Space Flight Center, Greenbelt, MD 20771, USA

Received 2018 September 7; revised 2018 October 29; accepted 2018 October 30; published 2018 November 30

Abstract

We present the analysis of the simultaneous high-resolution images from the *Hubble Space Telescope* and Keck adaptive optics system of the planetary event OGLE-2012-BLG-0950 that determine that the system consists of a $0.58 \pm 0.04\,M_{\odot}$ host star orbited by a $39 \pm 8\,M_{\oplus}$ planet at a projected separation of 2.54 ± 0.23 au. The planetary system is located at a distance of 2.19 ± 0.23 kpc from Earth. This is the second microlens planet beyond the snow line with a mass measured to be in the mass range 20–80 $M_{\oplus}$. The runaway gas accretion process of the core accretion model predicts fewer planets in this mass range. This is because giant planets are thought to be growing rapidly at these masses, and they rarely complete growth at this mass. So this result suggests that the core accretion theory may need revision. This analysis also demonstrates the techniques that will be used to measure the masses of planets and their host stars by the *WFIRST* exoplanet microlensing survey: one-dimensional microlensing parallax combined with the separation and brightness measurement of the unresolved source and host stars to yield multiple redundant constraints on the masses and distance of the planetary system.

Key words: gravitational lensing: micro – planetary systems

1. Introduction

Gravitational microlensing is currently the only technique to detect planets just outside the snow line (Gould & Loeb 1992) with masses as low as that of the Earth (Bennett & Rhie 1996). This method has so far discovered about 70 planets. For most events, the light-curve modeling of these microlensing exoplanets provides the planet–star mass ratio, but it does not provide the masses for either the planet or the host star. Bennett et al. (2007) showed theoretically that we can detect the foreground lens (host star and planet) and background source separately with high angular resolution follow-up observations taken a few years after the peak magnification, and these observations can determine the host star mass and distance. The planet mass is then determined from the microlensing light-curve determination of the planet–star mass ratio. High angular resolution follow-up observations of the planetary microlensing event OGLE-2005-BLG-169 using the *Hubble Space Telescope* (*HST*; Bennett et al. 2015) and Keck adaptive optics (AO) system (Batista et al. 2015) demonstrated this method and measured the masses and distance of this planetary system. These observations also confirmed the planetary interpretation of the microlensing light curve because the lens–source relative proper motion predicted from the planetary signal was consistent with the one measured by the follow-up observations. Earlier observations of microlens stars in the Galactic disk toward the Large Magellanic Cloud (LMC; Alcock et al. 2001; Gould et al. 2004) and the Galactic bulge (Kozlowski et al. 2007) provided earlier direct detections and mass measurements of microlens stars.

In addition to this event, there are a number of planetary microlensing events that have excess starlight detected at the position of the source in the high angular resolution follow-up observations. However, very few managed to measure the lens–source separation. Under the assumption that this excess flux is due to the planetary host star, a number of papers have claimed to determine the host star mass (Janczak et al. 2010; Kubas et al. 2012; Batista et al. 2014), but further follow-up observations by Bhattacharya et al. (2017) showed that the excess flux for one of these events was not due to the host star. A detailed analysis by Koshimoto et al. (2017a) indicated that excess starlight that is unresolved from the source can often be due to stars other than the lens, such as companions to the source or lens or unrelated stars. In cases where we were able to measure the microlensing parallax, we do not require confirmation of the predicted lens–source relative motion. Instead, high angular resolution follow-up observations that do not resolve the lens and source stars can confirm and refine the microlensing parallax mass measurement (Gaudi et al. 2008; Bennett et al. 2010b; Beaulieu et al. 2016, 2018) or distinguish between degenerate light-curve models (Bennett et al. 2016; Sumi et al. 2016).

The *Wide Field InfraRed Survey Telescope* (*WFIRST*) is NASA's next large astrophysics mission, following the *James Webb Space Telescope* (*JWST*). The *WFIRST* (Spergel et al. 2015) was created by the 2010 New Worlds New Horizons decadal survey to combine the science of three proposed science missions that all required a wide-field infrared space telescope. These missions were JDEM-Ω (Gehrels 2010), a dark energy mission, the Microlensing Planet Finder (Bennett et al. 2010a), and the Near Infrared Sky Surveyor. The *WFIRST* science program includes focused dark energy and microlensing exoplanet surveys and a significant guest observer component. A separate coronagraph instrument was added later to address the top medium-scale 2010 decadal survey priority. The goal of the *WFIRST* microlensing survey is to discover and characterize a large sample of cold, low-mass exoplanets with semimajor axes beyond roughly 1 au, which are largely impossible to detect with any other technique. This paper develops the exoplanet mass-measurement method that will be employed by *WFIRST*.

This paper presents the first result from the NASA Keck Key Strategic Mission Support (KSMS) program in support of *WFIRST*, entitled "Development of the *WFIRST* Exoplanet Mass Measurement Method," with follow-up observations of planetary microlensing event OGLE-2012-BLG-0950. This analysis demonstrates all of the methods that are expected to be the major host star and planet measurement methods for the *WFIRST* exoplanet microlensing survey (Bennett et al. 2007). The *HST* observations are part of a pilot program to use near-simultaneous observations with Keck and *HST* to measure the separation of the source and planet host stars using the color-dependent centroid shift method (Bennett et al. 2006) in the optical and infrared passbands. The Keck and *HST* images can be used separately to measure the source–host star separation using the image elongation method (Bennett et al. 2015). With the image elongation method, the lens and source are partially resolved such that their total point-spread function (PSF) is substantially elongated. So, in order to detect the lens, we need to fit multiple stellar profiles to the target. However, if the PSF is not substantially elongated, we can still detect the lens from the color-dependent centroid shift method. In this case, when the lens and source have very different colors, their relative brightness is very different in different passbands. As a result, the combination of the source+lens flux will have different centroids in different passbands at the same time. Hence, observing the target nearly simultaneously in three different passbands will give three different centroids for the same target. The shift of these centroids between different passbands can yield the separation and hence the detection of the lens. To demonstrate this method, we took a near-simultaneous observation of the event OGLE-2012-BLG-0950 with the *HST I* and *V* and Keck *K* passbands.

The microlensing event OGLE-2012-BLG-0950 (Koshimoto et al. 2017b) was observed by the microlensing survey telescopes of the Optical Gravitational Lensing Experiment (OGLE) and the Microlensing Observations in Astrophysics (MOA) collaborations. The anomaly at $\mathrm{HJD}' = (\mathrm{HJD}-2{,}450{,}000) = 6149$ was observed primarily in the MOA data, in addition to a single OGLE observation during the anomaly. No significant finite source effect from the background source was detected in the light-curve modeling, but a significant microlensing parallax signal was seen. However, as is often the case (Muraki et al. 2011), only a single component of the parallax vector ($\pi_{\mathrm{E,E}}$) was well measured with any precision. The second component ($\pi_{\mathrm{E,N}}$) is only constrained with an upper limit on $|\pi_{\mathrm{E,N}}|$. Koshimoto et al. (2017b) attempted to determine the mass of the lens system with the microlensing parallax measurement and the excess flux seen at the position of the source in 2013 AO follow-up imaging with the Keck NIRC2 camera, but the uncertainty in the $\pi_{\mathrm{E,N}}$ and the possibility that some or all of the excess flux could be due to a star other than the planetary host star, the masses of the host star, and its planet remained uncertain.

In this paper, we present the first planetary microlensing event in which the lens–source separation is measured that allows us to convert the one-dimensional microlensing parallax measurement to a complete microlensing parallax measurement (Ghosh et al. 2004). We combine this with the lens–source separation, measured in three passbands, to obtain a direct measurement of the lens system mass (Gould et al. 2004). The paper is organized as follows. Section 2 discusses the light-curve modeling, including modeling with constraints from the follow-up observations to determine the properties of the lens system. Section 3 describes the details of our high-resolution follow-up observations and their photometry calibrations. Section 4 focuses on the *HST* astrometric and photometric analyses with single- and dual-star PSF fits of the blended source plus lens target. Section 5 explores the astrometric and photometric analyses of Keck AO images. Section 6 describes the color-dependent centroid shifts between the positions of the blended source plus lens target in different passbands. In Sections 7 and 8, we determine the geocentric relative lens–source proper motions and show that the identification of the lens constrains the parallax vector. We discuss our determination of the exoplanet lens system parameters in Section 9 and the implications for similar measurements for *WFIRST* in Section 10. Finally, in Section 11, we summarize our conclusions and discuss the implications of this result for planet formation theory.

2. Light-curve Models

Our analysis includes constraints on the lens system from both the microlensing light curve and the high angular resolution follow-up observations, and we have found it most convenient to redo the light-curve analysis of this event that was previously presented by Koshimoto et al. (2017b). Our reanalysis uses the same data set used by Koshimoto et al. (2017b), except that the MOA-II survey light-curve data have been rereduced using the procedure described in Bond et al. (2017). This rereduction procedure includes a light-curve detrending procedure that is designed to remove systematic photometry errors due to the differential refraction of neighboring stars (Bennett et al. 2012), as well as other seeing and air-mass effects.

The modeling was done with the image-centered ray-shooting method (Bennett & Rhie 1996; Bennett 2010), and the results are summarized in Table 1. The parameters of these models can be separated into several categories. There are three parameters that are required for single-lens light curves: the Einstein radius crossing time, t_E; the time of closest lens–source alignment, t_0; and the lens–source separation at the time of closest alignment, u_0, which is dimensionless because it is given in units of the Einstein radius. For a binary lens system, t_0 and u_0 refer to the time of closest alignment between the source and the lens system center of mass. Four additional parameters are generally included to describe binary lens systems. These are the mass ratio, q, between the two lens masses; the angle, α, between the source trajectory and the

Table 1
Best-fit Unconstrained Model Parameters

	$u_0 < 0$		$u_0 > 0$		
Parameter	$s < 1$	$s \approx 1$	$s < 1$	$s \approx 1$	MCMC Averages
t_E (days)	70.823	71.059	70.093	70.062	69.8 ± 2.0
t_0 (HJD′)	6151.4951	6151.4988	6151.4805	6151.4785	6151.492 ± 0.028
u_0	−0.09764	−0.09734	0.09634	0.09648	0.004 ± 0.098
s	0.89915	1.00082	0.89937	1.00243	0.942 ± 0.056
α (rad)	−1.94169	−1.94301	1.94842	1.94873	−0.07 ± 1.95
$q \times 10^4$	1.6469	1.5668	1.6669	1.6295	1.95 ± 0.38
t_* (days)	0.03932	0.01433	0.01943	0.01324	0.057 ± 0.030
$\pi_{E,N}$	−0.2364	−0.2470	−0.2040	−0.2020	−0.09 ± 0.22
$\pi_{E,E}$	−0.1190	−0.1179	−0.0988	−0.1023	−0.122 ± 0.028
I_s	19.299	19.303	19.315	19.314	19.253 ± 0.038
V_s	20.807	20.810	20.823	20.821	20.762 ± 0.038
fit χ^2	6488.84	6490.48	6488.99	6490.60	

Table 2
Best-fit Model Parameters with $\boldsymbol{\mu}_{rel}$ and Magnitude Constraints

	$u_0 < 0$		$u_0 > 0$		
Parameter	$s < 1$	$s \approx 1$	$s < 1$	$s \approx 1$	MCMC Averages
t_E (days)	68.007	67.628	68.919	68.995	68.1 ± 1.2
t_0 (HJD′)	6151.4702	6151.4749	6151.4978	6151.4999	6151.484 ± 0.027
u_0	−0.09968	−0.09734	0.10088	0.10073	0.043 ± 0.091
s	0.89783	1.00136	0.89791	0.99900	0.928 ± 0.052
α (rad)	−1.94592	−1.94719	1.93987	1.94146	−0.84 ± 1.75
$q \times 10^4$	1.7255	1.7442	1.6726	1.6165	2.01 ± 0.39
t_* (days)	0.03634	0.03633	0.03609	0.01324	0.0366 ± 0.0013
$\pi_{E,N}$	0.2107	0.2103	0.2192	0.2178	0.213 ± 0.017
$\pi_{E,E}$	−0.1536	−0.1536	−0.1685	−0.1672	−0.157 ± 0.016
I_s	19.274	19.266	19.260	19.262	19.265 ± 0.023
V_s	20.783	20.773	20.768	20.769	20.734 ± 0.023
fit χ^2	6490.25	6491.87	6491.88	6493.45	

lens axis; the separation, s, between the two lens masses, in units of the Einstein radius; and the source radius crossing time, t_*, which is needed for most planetary events because the sharp planetary light-curve features often resolve the finite angular size of the source star. Finally, there are the two components of the microlensing parallax vector, $\pi_{E,N}$ and $\pi_{E,E}$, which describe the effect of the orbital motion of the observers on the Earth around the Sun.

As explained in the discovery paper (Koshimoto et al. 2017b), there are four degenerate solutions due to two well-known degeneracies. The first is the usual close–wide degeneracy that occurs for events that have planetary signals associated with the central caustic. Normally, the close–wide degeneracy relates models that differ mainly in the $s \leftrightarrow 1/s$ substitution, but in this case, with $s \sim 1$, the planetary caustics have merged with the central caustic, which ruins the usual $s \leftrightarrow 1/s$ relation. So the two solutions instead have $s \approx 0.9$ and 1.0. The second degeneracy is the well-known microlensing parallax degeneracy that involves a flipping of the orientation of the lens plane with respect to the orbit of the Earth. This is indicated by sign changes of the α and u_0 parameters.

One unexpected feature of this new analysis is that the best-fit $\pi_{E,N}$ value has changed sign from the discovery paper (Koshimoto et al. 2017b), from ∼0.12 to ∼−0.22, but in both cases, the uncertainty is quite large, as is often the case for ground-based microlensing parallax measurements (Muraki et al. 2011; Gould 2014). This change is due to an improvement in the detrending algorithm that we have applied to the MOA data, and it does not make a significant difference in our final conclusions.

In Section 8, we discuss constrained light-curve models that employ constraints on the lens and source star relative proper motion, $\boldsymbol{\mu}_{rel}$, and magnitudes that are derived in Sections 4, 5, and 7. The best-fit models from this analysis are shown in Table 2. As we discuss in Section 8, the $\boldsymbol{\mu}_{rel}$ constraint from our high angular resolution measurements greatly improves the precision of our $\pi_{E,N}$ measurements, which, in turn, enables precise determinations of the masses of the host star and planet.

The final column of Tables 1 and 2 gives the average of each parameter over Markov chain Monte Carlo (MCMC) calculations for all four models in weighted sums. In Table 1, this weighting is based only on the χ^2 difference ($\Delta\chi^2$) between the different models. Table 2 is based on separate Markov chains that include constraints from the follow-up observations. This is necessary because the constraints reduce the volume of parameter space by a large factor. Note that the probability distribution of the parameters u_0, s, and α have double peaks since they take significantly different values in the different degenerate models.

3. Follow-up Observations

The event OGLE-2012-BLG-0950 was observed with *HST* on 2018 May 22 (HJD′ = 8261.5, a difference of 2110 days or 5.78 yr from the peak of the magnification) with the Ultraviolet Visible Instrument of the Wide Field Camera 3 (WFC3-UVIS)

as part of the program GO-15455. Seven dithered images, each with 62 s exposure time, and eight dithered images, each with 111 s exposure time, were taken in the F814W and F555W passbands (which are the *HST* equivalent of the *I* and *V* bands), respectively. The pixel scale for the WFC3-UVIS instrument is ∼40 mas on a side. The images, corrected for charge transfer efficiency (CTE) losses (Anderson & Bedin 2010), were obtained from the Mikulski Archive for Space Telescopes (MAST) and reduced and stacked following the methods described in Anderson & King (2000, 2004). The stars from the *HST* stack images were matched and calibrated to the OGLE III catalog (Szymański et al. 2011), which is already calibrated to Cousins *I* (Cousins 1976) and Johnson *V* (Johnson 1966). Nine bright, isolated calibration stars with magnitude $I_{\rm OGLE_{III}} \leqslant 17.5$ and color $1.0 \leqslant (V-I)_{\rm OGLE_{III}} \leqslant 2.0$ were matched in both frames. We obtained the following calibration relations:

$$I_{\rm OGLE_{III}} = 28.764 + I_{\rm HST} + 0.0467(V-I)_{\rm HST} \pm 0.02, \quad (1)$$

$$V_{\rm OGLE_{III}} = 30.602 + V_{\rm HST} - 0.0641(V-I)_{\rm HST} \pm 0.03. \quad (2)$$

These uncertainties on the photometric calibration were estimated by dividing the rms scatter by the square root of the number of stars used for the transformation.

The same event was observed within a day of the *HST* observations with the Keck AO NIRC2 instrument using a laser guide star during the early morning of 2018 May 23 as part of our Keck NASA KSMS program. Five dithered exposures, each of 30 s, were taken in the K_S short passband with the wide camera. In this paper, from now on, we refer to the K_S band as the *K* band. Each wide camera image covers a 1048 × 1048 square pixel area, and each pixel size is about 40 × 40 mas^2. These images were flat field– and dark current–corrected using standard methods and then stacked using the SWarp Astrometics package (Bertin et al. 2002). The details of our methods are described in Batista et al. (2014). We performed aperture photometry on these wide camera images using the SExtractor code (Bertin & Arnouts 1996). These wide images were used to detect and match as many bright isolated stars as possible to our custom reduction (Beaulieu et al. 2016) of the VVV images (Minniti et al. 2010) that is calibrated to 2MASS (Carpenter 2001). Twenty-seven isolated bright stars in the *K* band were calibrated to VVV with a 0.02 mag dispersion.

On the same night as the wide camera images, this event was observed with the NIRC2 narrow camera in the *K* band using laser guide star AO (LGSAO). The main purpose of these images is to obtain images with a sharp, well-characterized PSF for the astrometric and photometric analysis of the lens and source stars (see Section 5). Thirty-nine dithered observations were taken with 60 s exposures. The images were taken with a small dither of 0.″7 at a position angle (P.A.) of 0° with each frame consisting of two coadded 30 s integrations. The observations were taken in eight dither positions with at least four images in each dither position. The natural seeing for these narrow camera images was ∼0.″4–0.″6. There are 1048 × 1048 pixels in each image, with each pixel subtending 10 mas on each side. The stars from the narrow camera images were cross-matched to the wide camera photometry for calibration. The photometry used for narrow camera images is from the DAOPHOT analysis described in Section 5.

4. *HST* ePSF Fitting

Like many other space telescope cameras, the *HST* WFC3-UVIS pixel scale undersamples the PSF. This is a compromise between field of view and angular resolution. Fortunately, accurate photometry (Lauer 1999) and astrometry (Anderson & King 2000) can still be obtained if the image pointings are dithered to recover the spatial sampling lost to undersampling. To overcome this problem, we adopt the method of Anderson & King (2006) to construct an effective PSF (ePSF) from the dithered images. This method has proved effective at measuring the separation of stars separated by <1 FWHM (Bennett et al. 2015; Bhattacharya et al. 2017). The full *HST* analysis is done using only the distortion-corrected individual undersampled dithered images. The 100× oversampled image shown in Figure 1 is produced at the end of the analysis for visual inspection. Eight main-sequence stars, within a 120 pixel radius of the target and similar brightness as the target, were chosen to build the ePSF. The ePSFs of all eight stars were computed in each image frame, then the average ePSF over all the frames was obtained. It is this averaging of the ePSFs from all dithered images that helps to overcome the undersampling problem. The procedure was iterated until the average ePSFs converged. We used this final ePSF model to fit single and dual stellar profiles for our target object as described in the next paragraphs. Our methodology for fitting single and multiple stellar profiles with ePSFs is described in detail in Bhattacharya et al. (2017). The FWHMs of the ePSFs in the *I* and *V* bands are 76 and 72 mas, respectively.

The first step of ePSF modeling is to do a single-star fit of our target object. There are three model parameters for such a fit: the two-dimensional position of the star and the stellar flux. We selected a region centered on the target that included 175 pixels from our seven *I*-band images and 200 pixels from our eight *V*-band images. The calibrated magnitudes of the target object from the best-fit solution were 18.64 ± 0.02 and 20.41 ± 0.03 in the *I* and *V* bands, respectively. The magnitude uncertainties are the combination of the ePSF fitting and calibration uncertainties. As Figure 1 shows, the residual image from this fit indicates that the best single-star fit is a poor fit. It is also clear that the *I* and *V* magnitudes of the target are significantly brighter than the source magnitude determined from the microlensing light-curve analysis: $I_S = 19.26 \pm 0.05$ and $V_S = 20.65 \pm 0.07$. This indicates the presence of at least one additional star blended with the source star, so we proceed with the dual-star ePSF fitting analyses described below.

The dual-star ePSF fitting method requires six model parameters: the two-dimensional positions of each of the stars (x_1, y_1, x_2, y_2), the total flux (Z), and the flux fraction (f_1) of star #1. The first stage of our dual-star fitting process is a grid search. The positions of each star were allowed to explore the full grid of 151 and 200 pixels for the *I* and *V* bands with a step size of 0.02 pixel. For each combination of positions of the two stars, the flux fraction, f_1, was varied between 0.0 and 1.0 with a step size of 0.02. At each step, the χ^2 value was computed, and the minimum χ^2 solution was stored. This dense grid search yielded our first best-fit result on the dual-star ePSF fit. The grid search was performed to cover the full parameter space. The best-fit result was used as an initial condition for an MCMC (Verde et al. 2003) ePSF fitting in order to obtain a more precise measurement with error bars. Our detailed methodology of MCMC ePSF fitting for multiple stars is described in detail in Bhattacharya et al. (2017). The best-fit photometry from the dual-star MCMC PSF models is shown in Table 3, and the best-fit relative astrometry is shown in Figure 4. The uncertainties are determined from the distribution

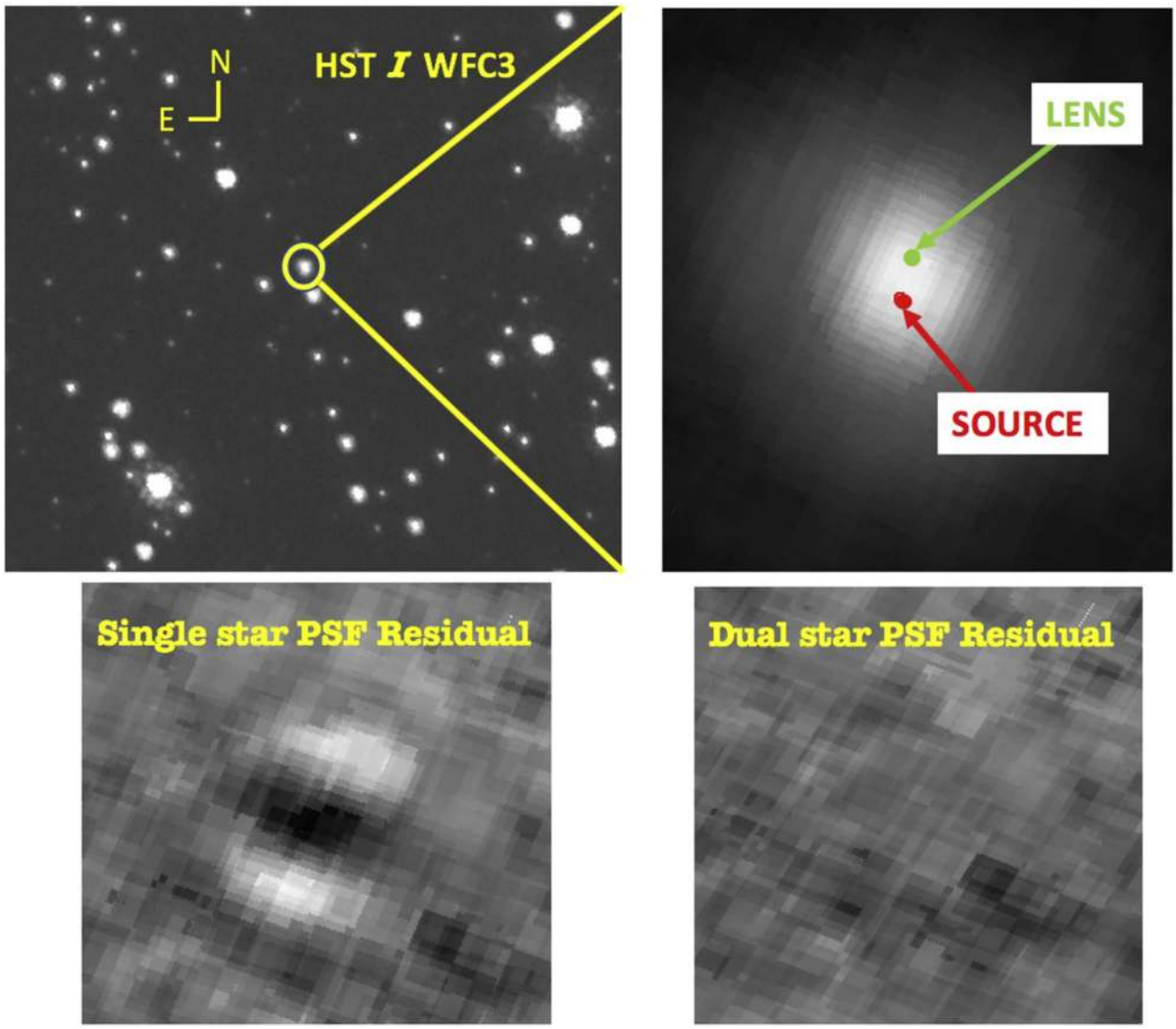

Figure 1. Top left: stack image in the *HST I* (F814W) passband with the target indicated by the yellow circle. Top right: summed image of all the individual images of the target object. The source and lens positions obtained from the best-fit dual-star PSF model to the individual images. Bottom left: residual image from the best-fit single-star PSF model. The wings are undersubtracted and the core is oversubtracted, indicating that the best-fit single-star PSF model is not consistent with the flux distribution of the target object. Bottom right: residual image from the best-fit dual-star PSF model. This indicates a much better fit consistent with Poisson noise (which is larger at the location of the subtracted stars), so the best-fit dual-star model is compatible with the flux distribution of the target. Both of the bottom images are demonstrated using the same photometry scale.

of 29,727 and 37,132 accepted MCMC links in the I and V bands, respectively. Figure 2 shows that the correlation between parameters, lens flux contribution, and lens–source separation are negligible in the I band but quite strong in the V band. This justifies the calculation of the uncertainties of these correlated parameters from the MCMC chains instead of calculating the uncertainties on individual parameters separately. The residual of the dual star shown in Figure 1 shows that it is a good model.

The dual-star ePSF model results (Table 4) show that the target consists of two stars with a separation of ∼34 mas, with consistent separations measured in all three passbands. The magnitudes of star #1 (the southernmost star) are $I_1 = 19.24 \pm 0.06$ and $V_1 = 20.65 \pm 0.09$, and the magnitudes of the second star are $I_2 = 19.57 \pm 0.09$ and $V_2 = 22.27 \pm 0.21$. Star #1 has color $V_1 - I_1 = 1.41 \pm 0.1$, and star #2 has color $V_2 - I_2 = 2.70 \pm 0.23$. Star #1 is bluer than star #2. Since both stars have similar brightnesses in the I band and the lens is located nearer than the source in the bulge, the lens should be redder than the main-sequence source. Since star #1 is bluer and also significantly brighter in the V band, we identify star #1 as the source. Also, the

Table 3
Photometry from Dual-star PSF Fits

Star	Passband	Mag
Lens	*HST I*	19.57 ± 0.09
	HST V	22.27 ± 0.21
	Keck *K*	17.27 ± 0.04
Source	*HST I*	19.24 ± 0.06
	HST V	20.65 ± 0.09
	Keck *K*	17.68 ± 0.05

Note. Magnitudes are calibrated Cousins *I*-band, Johnson *V*-band, and 2MASS *K*-band magnitudes.

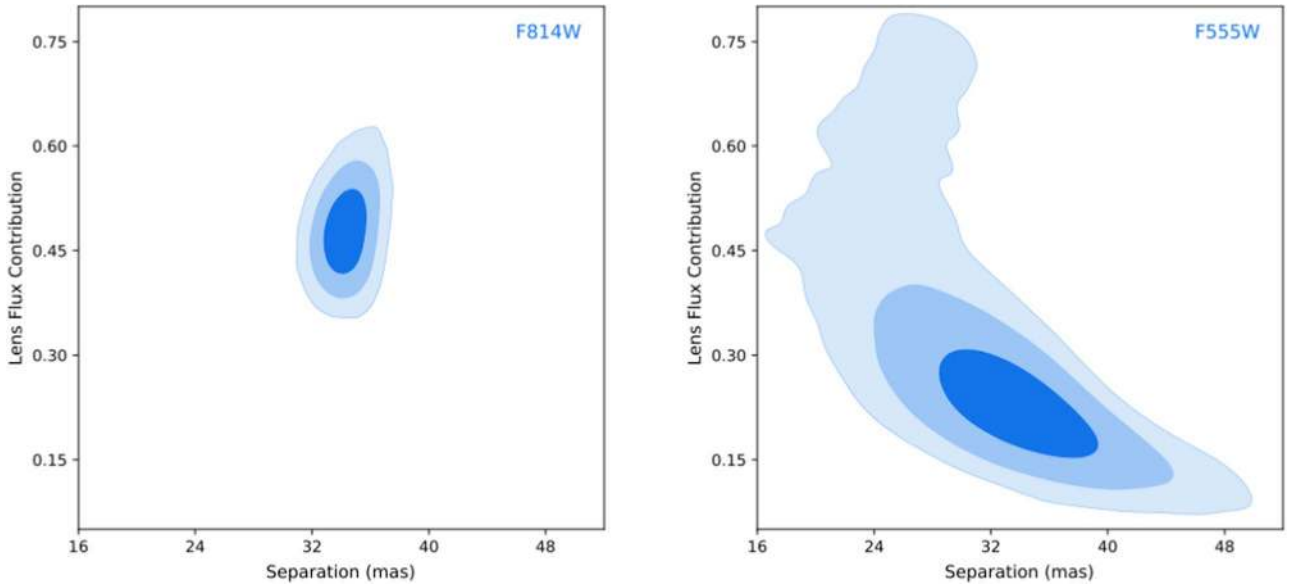

Figure 2. Left: lens flux contribution in the *HST I* (F814W) passband with respect to the lens–source separation. Right: lens flux contribution in the *HST V* (F555W) passband with respect to the lens–source separation. These plots are made from the MCMC chains of dual-star PSF fitting mentioned in Section 4. The three contours, from darker to lighter shades, represent the 68.5%, 97%, and 99% confidence levels. The correlation between the lens flux contribution and the lens–source separation is almost negligible in the *I* band. However, in the *V* band, these two parameters are more strongly correlated. This justifies calculation of the uncertainties from the MCMC chains instead of calculating the uncertainties on each individual parameter separately.

Table 4
Measured Lens–source Separation and Relative Proper Motion

Passband	Separation (mas)		$\mu_{rel,H}$ (mas yr^{-1})	
	East	North	East	North
HST I	-15.5 ± 0.4	30.5 ± 0.7	-2.68 ± 0.05	5.28 ± 0.13
HST V	-15.6 ± 1.4	30.8 ± 2.6	-2.70 ± 0.27	5.33 ± 0.47
Keck *K*	-15.9 ± 2.9	29.3 ± 3.0	-2.75 ± 0.49	5.07 ± 0.52

I and *V* magnitudes for star #1 match the approximately calibrated source magnitudes (Koshimoto et al. 2017b), and they are within 1σ of the source brightness predicted from our light-curve modeling based on improved MOA photometry, as indicated in Table 1. In contrast, star #2 does not match with the predicted source flux from the light curve of $I_S = 19.24 \pm 0.03$ and $V_S = 20.65 \pm 0.07$. Hence, the second star is a candidate for the planetary host and lens star. Note that this event also had a one-dimensional parallax measurement from light-curve modeling; this tells us whether the lens would be to the east or west of the source in the high-resolution follow-up images. If the high-resolution follow-up image shows only the lens and the source, the source can be identified using this abovementioned information from the one-dimensional parallax as well.

The lens–source separations in both the east and north directions are consistent in our independent analysis of the *I* and *V* passbands. The separation of these two stars is also measured to high precision. The one-dimensional separation as measured in the *I* band is 34.21 ± 0.65 mas, which is a precision of 2%, even though the separation is <0.5 FWHM of the PSF. This is consistent with our previous analysis of the event MOA-2008-BLG-310, where we were able to measure the separation between the source and blend star (which was not the lens) to a precision of 15% when the separation was 14 mas (Bhattacharya et al. 2017). From Koshimoto et al. (2017b), the upper limit of the separation at 5.78 yr predicted from the geocentric relative lens–source proper motion is 38.73 mas. As described in Section 9, the upper and lower limits on lens–source separation calculated from the geocentric relative proper motion are 34.2 and 43.8 mas. The one-dimensional separations measured in the *I* and *V* passbands are 34.21 ± 0.65 and 34.53 ± 2.40 mas, respectively. These measured separations are consistent with the upper and lower limits of separations from Section 9, as well as the upper limit of the predicted separation from Koshimoto et al. (2017b).

5. Keck AO PSF Fitting

Thirty-nine images taken with the Keck NIRC2 narrow camera were reduced. These images taken with the narrow camera are not undersampled, so we did not need to adopt the ePSF method for the analysis of these images. For the reduction of these images, we used *K*-band dome flats taken with the narrow camera on the same day as the science images. There were five dome-flat images with the lamp on and five more images with the lamp off, each with 65 s exposure time. Also, at the end of the night, we took 20 sky images using a clear patch of sky at an (R.A., decl.) of (18:08:04.62, −29:43:53.7) with an exposure time of 30 s each. All of these images were used to flat-field, bias-subtract, and remove bad pixels and cosmic rays from the 39 raw science images. Finally, these clean raw images were stacked into one image that we used for the final photometry and astrometry analysis.

Because the source and candidate lens stars are separated by <1 FWHM, we must analyze the Keck data with a PSF fitting code to measure the astrometry and photometry of this two-star system. However, PSF fitting photometry codes that employ analytic PSF models may have problems with AO images that often have highly non-Gaussian PSFs. We have previously found that DAOPHOT (Stetson 1987) does quite well with such images (Bennett et al. 2010b), so we use DAOPHOT for the analysis of our OGLE-2012-BLG-0950 Keck data.

To start our analysis, we needed to construct a proper PSF. We built the PSF in three stages. In the first stage, we ran the

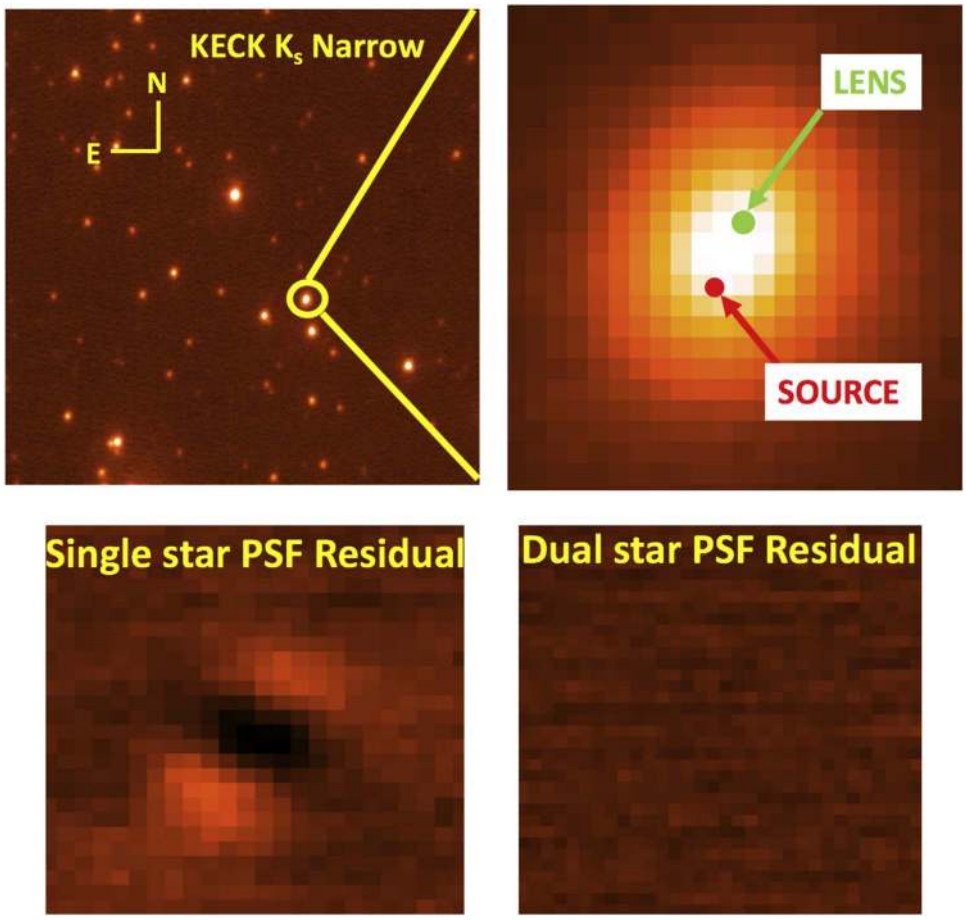

Figure 3. Top left: stack image of 39 Keck *K*-band images taken with the narrow camera. The target is indicated by the yellow circle. Top right: closer look at the target object. The source and lens positions are obtained from the best-fit dual-star PSF model. Bottom left: residual image after subtracting the best-fit single-star PSF model. The undersubtracted wings and oversubtracted core indicate that the best-fit single-star PSF model is not consistent with the data. Bottom right: residual image after subtracting the best-fit dual-star PSF model. This shows only noise, which implies that the best-fit dual-star model can account for the flux distribution of the target. Both of the bottom images use the same photometry scale.

FIND and PHOTOMETRY commands of DAOPHOT to find all the possible stars in the image. Then we used the PICK command to find 23 bright ($K < 19.24$) isolated stars to be used for constructing our PSF. Our target object was excluded from this list of PSF stars because it is expected to consist of two stars that are not in the same position. We built a PSF from these stars and fit all the stars in the field with this PSF. In the second stage, we carefully checked the residual image that has all the identified stars subtracted. We noticed several stars that had large residuals. These were either very bright stars that were near saturation (where the detector becomes nonlinear) or elongated PSFs due to multiple blended stellar images. At this stage, we carefully checked and found that two of our PSF contributing stars had a significant residual from the PSF subtraction. A close look showed that both of these had slight elongations that are probably due to binary companions. So these two stars were removed from our PSF star list, and the PSF was constructed again. Next, we ran the PSF fitting again on the field with the new PSF and moved on to the third stage. In the third stage, we removed all of the neighbor stars of the PSF stars and computed a clean final PSF from these 21 stars. We then did a final round of PSF fitting for all stars in the image with this clean PSF.

After finding a good PSF model, we started our analysis with a single-star PSF fit to the target object. The residual of this fit is shown in Figure 3. This residual shows a clear pattern that indicates that it is elongated compared to the PSFs of single stars. From our reanalysis of this event (with improved MOA photometry), we find an extinction-corrected magnitude and color of the source star $I_{S,0} = 18.40 \pm 0.07$ and $(V - I)_{S,0} = 0.74 \pm 0.07$, which is consistent with the Koshimoto et al. (2017b) analysis. From the color–color relation in Kenyon & Hartmann (1995), $(V - I)_{S,0} = 0.74$ corresponds to the dereddened color $(I - K)_{S,0} = 0.75$. From Cardelli et al. (1989), the extinction in the *K* band is $A_K = 0.12$ at 8.2 kpc (see Section 9). Hence, the source *K*-band calibrated magnitude is $(18.40 - 0.75 + 0.12) \pm 0.07 = 17.77 \pm 0.07$.

The total measured *K*-band magnitude from our single-star fit is 16.71 ± 0.03, which implies an excess flux of $K = 17.22$ mag on top of the source. This excess flux, combined with the residual shown in the lower left panel of Figure 3, implies that we should proceed with dual-star PSF fitting for this target. In the dual-star fit, DAOPHOT allowed the star positions to move around up to a 30 mas or 3 pixel radius from their initial positions. In the *HST* astrometry analysis (Section 4), we found that the separation between the two stars is ∼34 mas. So, limiting the movement of the star positions to $\leqslant$30 pixels should not impede our dual-star modeling. The best dual-star fit yielded two stars with calibrated *K* magnitudes of 17.27 ± 0.04 and 17.68 ± 0.05, as listed in Table 3, which matches the predicted source brightness from the discovery paper. The separation of these two stars, given in Table 4, is consistent

Table 5
Blended Lens + Source Centroid Shifts

	Single-Star		Dual-Star		Single-Star—Dual-Star	
Passbands	ΔE (mas)	ΔN (mas)	ΔE (mas)	ΔN (mas)	ΔE (mas)	ΔN (mas)
$V-I$	−3.764	7.249	−3.460	5.950	−0.304	1.299
$V-K_S$	−6.400	12.324	−6.815	13.358	0.415	−1.034
$I-K_S$	−2.635	5.074	−5.709	7.863	3.074	−2.789

with their separations in the *HST I* and *V* bands. Both the single- and dual-star fits were done using the Newton–Raphson method following Stetson (1987). The uncertainties were calculated following King (1983),

$$\sigma_x = 0.65238 \times \mathrm{FWHM} \times \sqrt{\frac{4}{3}} \times \frac{\sigma_F}{F}, \quad (3)$$

where F is the flux of the respective star. The uncertainty in the y direction can be presented by the same equation. The FWHM of the *K*-band narrow image measured from DAOPHOT is 84 and 87 mas in the x and y directions.

6. Color-dependent Centroid Shift with Simultaneous *HST* and Keck Observations

The color-dependent centroid shift is a method that can be used to confirm the identification of excess blended flux on top of the source with the lens star. This is possible because the constraints on the properties of the blended image of the lens and source are known from the microlensing light curve. These known properties always include the source star brightness, and they usually include the lens–source relative proper motion, $\mu_{\rm rel}$, or the microlensing parallax, π_E.

The source stars are biased toward the brightest stars in the bulge, since a brighter source provides a stronger microlensing signal. However, the lens stars are detected with a microlensing rate that scales as lens mass, $M_L^{0.5}$, a mass function that scales as $M_L^{-1.3}$, and a detection efficiency that scales as M_L^n, where $0 \leqslant n \leqslant 0.5$, which implies a much flatter distribution. Thus, the lens stars tend to have a lower mass with a redder color than the source stars, as the cases of OGLE-2005-BLG-169 (Batista et al. 2015; Bennett et al. 2015) and OGLE-2012-BLG-0950, presented in this paper, demonstrate.

When the source and lens stars have different colors, their blended images will have different centroids in follow-up images in different passbands due to the separation between the lens and source. This is the color-dependent centroid shift, which was first demonstrated for the first planet found by microlensing (Bennett et al. 2006) using *HST* data. The time interval between the magnification peak and the high-resolution follow up is denoted by Δt. The main advantage of this method over the measurement of image elongation is that the S/N of the color-dependent centroid-shift scales as, Δt, whereas the image elongation signal grows as Δt^2 if the source brightness is known or Δt^3 when the source brightness is not constrained (Bennett et al. 2007). Thus, the color-dependent centroid method might be the most effective method for determining the lens–source separation when the separation is small.

The color-dependent centroid shift is largest with the maximum color difference between passbands, and this was the justification for the near-simultaneous *HST* and Keck AO imaging. Previous studies (Lu et al. 2014) have argued that it is possible to obtain astrometry with an accuracy of 150 mas from Keck NIRC2 images, but this requires a large number of careful corrections. Since our primary science result comes from the dual-star fits, we do not require this very high precision astrometry for our science results. So, we present a preliminary test of the color-dependent centroid method here.

In order to measure the color-dependent centroid shift between each pair of passbands, we must perform a coordinate transformation between the images in the different passbands. We have corrected the Keck data for achromatic differential refraction (Yelda et al. 2010) and geometric distortion (Service et al. 2016). Based on Gubler & Tytler (1998), the chromatic differential refraction effect would be <0.2 mas. Hence, this effect is ignored for our preliminary analysis. (The *HST* data were corrected for geometric distortion by standard methods; Kozhurina-Platais 2012.) For our preliminary analysis, we have performed linear coordinate transformations with a relatively small number of stars around the target. For the *HST I* to Keck *K* transformation, we used 10 stars, which resulted in a one-dimensional rms scatter of 0.9 mas. For the *HST V* to Keck *K* transformation, we used eight stars with a one-dimensional rms scatter of 1.3 mas. Finally, for the *HST I* to *HST V* transformation, we used 19 stars with an rms scatter of 0.2 mas, which is consistent with the astrometric precision obtained in a previous attempt to measure the color-dependent centroid shift (Bennett et al. 2006). These coordinate transformations were used to compare the centroids of the blended lens plus source image from the single PSF fits, and these results are reported in the second and third columns of Table 5. The color-dependent centroid shifts in different passbands are demonstrated in Figure 4.

We can also use our dual-star fits from Sections 4 and 5 to calculate the expected color-dependent centroid shifts. From Section 4, the flux fraction of the source (or star #1) is f_1, which implies that the flux fraction of the excess flux is $(1-f_1)$. For the remainder of this section, we will refer to this excess flux as being due to the lens star (see Section 9 and Figure 6). We denote the source position vector as $\boldsymbol{x}_1$ and the lens position as $\boldsymbol{x}_2$. The lens–source separation is given by $\Delta\boldsymbol{x}_{\rm L-S}$. For a passband i, the centroid of the combined source and the lens flux, $\boldsymbol{x}_{c,i}$, is given by

$$\boldsymbol{x}_{c,i} = f_{1,i}\boldsymbol{x}_1 + (1 - f_{1,i})\boldsymbol{x}_2, \quad (4)$$

$$\boldsymbol{x}_2 = \boldsymbol{x}_1 + \Delta\boldsymbol{x}_{\rm L-S}, \quad (5)$$

$$\boldsymbol{x}_{c,i} = f_{1,i}\boldsymbol{x}_1 + (1 - f_{1,i})(\boldsymbol{x}_1 + \Delta\boldsymbol{x}_{\rm L-S}). \quad (6)$$

For a different passband, $j \neq i$, the centroid of the blended source plus lens image is given by

$$\boldsymbol{x}_{c,j} = f_{1,j}\boldsymbol{x}_1 + (1 - f_{1,j})(\boldsymbol{x}_1 + \Delta\boldsymbol{x}_{\rm L-S}). \quad (7)$$

Subtracting Equation (6) from Equation (7), we obtain the centroid shift between passbands j and i as shown in

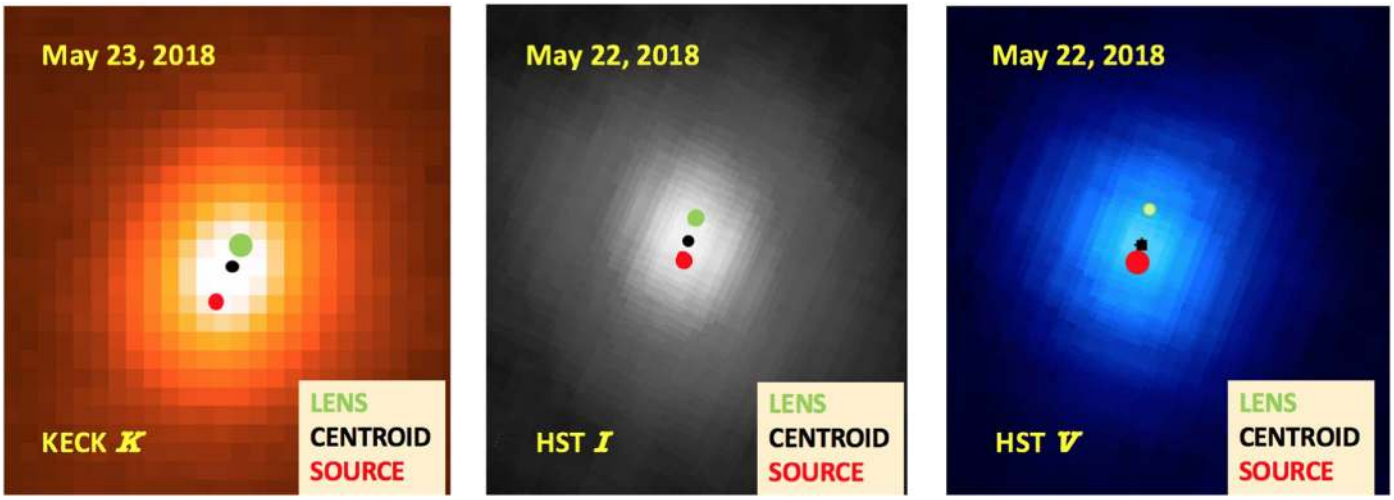

Figure 4. The blended image of the source plus lens stars is shown in three different passbands: Keck *K* (left), *HST I* (middle), and *HST V* (right). The source and lens positions, determined from the best-fit dual-star PSF models, are shown with red and green dots, respectively. The centroids are calculated according to the flux of the lens and source in the respective passbands (from Table 3). The sizes of the source and lens dots are proportional to the flux fraction for the lens and source stars. In the Keck *K* band, the lens is brighter than the source, hence the green dot is bigger than the red dot and the centroid is shifted toward the lens. In the *I* band, the source is slightly brighter than the lens, so the centroid is slightly closer to the source. In the *V* band, the centroid is moved toward the source, since the source is much brighter than the lens.

Equation (8). Rearranging the terms, we can derive the lens–source separation from this centroid shift and the flux ratios in two different passbands:

$$\Delta \boldsymbol{x}_{c,(j,i)} = \boldsymbol{x}_{\rm l}(f_{{\rm l},j} - f_{{\rm l},i}) + (f_{{\rm l},i} - f_{{\rm l},j})(\boldsymbol{x}_{\rm l} + \Delta \boldsymbol{x}_{\rm L-S}), \quad (8)$$

$$\Delta \boldsymbol{x}_{c,(j,i)} = (f_{{\rm l},i} - f_{{\rm l},j})\Delta \boldsymbol{x}_{\rm L-S}, \quad (9)$$

$$\Delta \boldsymbol{x}_{\rm L-S} = \frac{\Delta \boldsymbol{x}_{c,(j,i)}}{(f_{{\rm l},i} - f_{{\rm l},j})}. \quad (10)$$

We can now use Equation (9) to predict the color-dependent centroid shifts from the dual-star fits. The results are shown in the fourth and fifth columns of Table 5. The sixth and seventh columns of this table show the difference between these two predictions. The centroid shift estimate from the dual-star fits seems to be a rough match to the centroid measurements from the single-star fits, but the differences between the single-star fit measurements and the dual-star fit estimates are much larger than we would like if we are to use the color-dependent centroid shift measurement to confirm lens–source separation predictions at small separations. We expect an astrometric precision in each of the passbands of ∼0.3 mas to be achievable (Bennett et al. 2006; Lu et al. 2014), so we should be able to achieve a relative astrometric precision of $\lesssim$0.5 mas between pairs of passbands. However, based on the scatter in our transformations between passbands, it is clear that this is only possible between the *HST V* and *I* bands. Our transformations between the *HST* passbands and the Keck *K* band have a one-dimensional scatter of $\gtrsim$1 mas, so submilliarcsecond precision is not possible until these transformations are improved. Fortunately, there are several ways in which these transformations can be improved. We will study this issue more completely in a future paper.

We should note that the lens–source separation of 34 mas could be too large for Equations (4)–(10) to apply, particularly in the *HST V* band with a PSF FWHM of ∼48 mas. Thus, the comparison shown in Table 5 might not be completely fair. From Table 3, we can conclude that the positions of the lens derived from the single-star fit would be different by ∼10%–20% from the measured positions of the lens using dual fits. Hence, the large elongation may explain why this centroid shift method does not match the dual-star fit results more closely.

7. Determination of Relative Lens–source Proper Motion

Our high-resolution observations were taken 5.83 yr after the microlensing event magnification peak. If these images were taken 6 yr after the microlensing magnification, then the *HST* frame would have coincided with the heliocentric frame. However, this time difference of 0.17 yr between the heliocentric frame and our current *HST* frame, with a lens system at 2.1 kpc (see Section 9), produces a less than 1σ difference in the lens–source separation. So, we approximate the *HST* frame to the heliocentric frame. At the time of peak magnification, the separation between lens and source was $\sim u_0\theta_E \sim 0.1$ mas. Hence, by dividing the measured separation by the time interval 5.78 yr, we obtain the heliocentric lens–source relative proper motion, $\boldsymbol{\mu}_{\rm rel,H}$. A comparison of the $\boldsymbol{\mu}_{\rm rel,H}$ values from our independent dual-star fits is shown in Table 4. From our *I*-band measurements, we find that ($\mu_{\rm rel,H,l}$, $\mu_{\rm rel,H,b}$) = (3.23, 4.84) mas yr^{-1} in galactic coordinates, and the amplitude of $\mu_{\rm rel,H} = 5.92 \pm 0.12$ at an angle of ∼57° from the direction of Galactic rotation. The dispersion in the motion of stars in the local Galactic disk is ∼30 km s^{-1}, which corresponds to a proper-motion dispersion of ∼3 mas yr^{-1} (in both directions) at the lens distance of $D_{\rm L} \approx 2.1$ kpc, as presented in Section 9. The source is in the bulge, with a proper-motion dispersion of ∼2.5 mas yr^{-1} in each direction. Thus, the measured $\boldsymbol{\mu}_{\rm rel,H}$ is entirely consistent with the combination of the mean relative proper motion of 6 mas yr^{-1} in the direction of Galactic rotation combined with the proper-motion dispersion of bulge source and disk lens stars.

Our light-curve models were done in a geocentric reference frame that differs from the heliocentric frame by the instantaneous velocity of the Earth at the time of peak magnification, because the light-curve parameters can be determined most precisely in this frame. However, this also

means that the lens–source relative proper motion that we measure with follow-up observations is not in the same reference frame as the light-curve parameters. This is an important issue because, as we show below, the measured relative proper motion can be combined with the microlensing parallax light-curve parameter to determine the mass of the lens system. The relation between the relative proper motions in the heliocentric and geocentric coordinate systems is given by (Dong et al. 2009)

$$\boldsymbol{\mu}_{\rm rel,H} = \boldsymbol{\mu}_{\rm rel,G} + \frac{\boldsymbol{v}_{\oplus}\pi_{\rm rel}}{\rm au}, \tag{11}$$

where $\boldsymbol{v}_{\oplus}$ is the projected velocity of the Earth relative to the Sun (perpendicular to the line of sight) at the time of peak magnification. The projected velocity for OGLE-2012-BLG-0950 is $\boldsymbol{v}_{\oplus \rm E,N} = (4.096,\ -0.448)\,{\rm au\,yr^{-1}}$ at the peak of the microlensing, HJD′ = 6151.48. The relative parallax is defined as $\pi_{\rm rel} \equiv 1/D_L - 1/D_S$, where D_L and D_S are the lens and source distances. Hence, Equation (11) can be written as

$$\boldsymbol{\mu}_{\rm rel,G} = \boldsymbol{\mu}_{\rm rel,H} - (4.096,\ -0.448) \times (1/D_L - 1/D_S).$$

Since $\boldsymbol{\mu}_{\rm rel,H}$ is already measured in Table 4, Equation (11) represents the geocentric relative proper motion, $\boldsymbol{\mu}_{\rm rel,G}$, as a function of the lens distance. Now, at each possible lens distance, we can use the $\mu_{\rm rel,G}$ value from Equation (11) to determine the angular Einstein radius, $\theta_E = \mu_{\rm rel,G} t_E$. As we explain below, $\boldsymbol{\mu}_{\rm rel,G}$ can also be used to convert a one-dimensional microlensing parallax measurement into a full measurement of the microlensing parallax vector. The three lens flux measurements in the *V*, *I*, and *K* bands and the one-dimensional parallax measurement constrain the angular Einstein radius and microlensing parallax vector and, therefore, the mass and distance of the lens.

8. $\boldsymbol{\mu}_{\rm rel,H}$ and Lens Flux Constraints on $\boldsymbol{\pi}_{\rm E}$ and Light-curve Models

The OGLE-2012-BLG-0950 light curve shows a significant improvement of $\Delta\chi^2 = 85.9$ due to the measurement of the microlensing parallax effect. But, as is often the case (Muraki et al. 2011; Gould 2014), only the $\pi_{E,E}$ component of the microlensing parallax vector is measured precisely. As shown in the left panel of Figure 5, the 2σ range for $\pi_{E,N}$ is $-0.39 < \pi_{E,N} < 0.43$. However, the microlensing parallax vector, $\boldsymbol{\pi}_{\rm E}$, is parallel to the $\boldsymbol{\mu}_{\rm rel,G}$ vector, and the two quantities are related by

$$\boldsymbol{\pi}_{\rm E} = \frac{\pi_{\rm rel}}{t_{\rm E}} \frac{\boldsymbol{\mu}_{\rm rel,G}}{|\ \mu_{\rm rel,G}|^2}. \tag{12}$$

So, with measurements of $\pi_{E,E}$ and $\boldsymbol{\mu}_{\rm rel,H}$, we can use Equations (11) and (12) to solve for $\pi_{E,N}$ (Ghosh et al. 2004; Bennett et al. 2007). Gould (2014) showed that Equations (11) and (12) can be converted to a quadratic equation in $\pi_{E,N}$. A quadratic equation means two solutions, and Gould argued that this presented an important degeneracy that could lead to an ambiguous interpretation, but we find that this is generally not the case. For our measured value of $\boldsymbol{\mu}_{\rm rel,H}$, the degenerate solutions require that one solution had $\pi_{\rm rel} < 0$, which would imply that the lens is (unphysically) more distant than the source. So, there is a unique solution in the case of OGLE-2012-BLG-0950. If the sign of $\boldsymbol{\mu}_{\rm rel,H}$ was reversed, then there would be some degeneracy in the $\pi_{E,E}$ values at large $|\pi_{E,E}|$, but these would only be important for $D_L < 0.08$ kpc. In general, this degeneracy is not important when $|\boldsymbol{\mu}_{\rm rel,H}| \gg |\boldsymbol{v}_{\oplus}\pi_{\rm rel}/{\rm au}|$, as is the case for virtually all microlensing events observed toward the Galactic bulge.

In order to obtain good sampling of light curves that are consistent with our constraints, we apply constraints inside our modeling code to ensure that the heliocentric proper motion and lens magnitudes are consistent with the Keck and *HST* observations. These constraints are the $\mu_{\rm rel,H,N}$ and $\mu_{\rm rel,H,E}$ values given in Table 4, as well as $V_L = 22.18 \pm 0.26$, $I_L = 19.51 \pm 0.09$, and $K_L = 17.21 \pm 0.14$. They are implemented by calculating a χ^2 contribution from each of the constraints and adding it to the light-curve fit χ^2 inside the modeling code (Bennett 2010). This requires the use of a mass–luminosity relation. As argued in Bennett et al. (2018), an empirical mass–luminosity relation is preferred for lens masses $\lesssim 0.7\,M_\odot$. Following Bennett et al. (2018), we use a combination of mass–luminosity relations for different masses. For $M_L \geqslant 0.66\,M_\odot$, $0.54\,M_\odot \geqslant M_L \geqslant 0.12\,M_\odot$, and $0.10\,M_\odot \geqslant M_L \geqslant 0.07\,M_\odot$, we use the relations of Henry & McCarthy (1993), Delfosse et al. (2000), and Henry et al. (1999), respectively. Between these mass ranges, we linearly interpolate between the two relations used on the boundaries. That is, we interpolate between the Henry & McCarthy (1993) and the Delfosse et al. (2000) relations for $0.66\,M_\odot > M_L > 0.54\,M_\odot$, and we interpolate between the Delfosse et al. (2000) and Henry et al. (1999) relations for $0.12\,M_\odot > M_L > 0.10\,M_\odot$.

For the mass–luminosity relations, we must also consider the foreground extinction. At a Galactic latitude of $b = -4°.634$ and lens distance of ∼2 kpc, the lens system is likely to be behind some, but not all, of the dust that is in the foreground of the source. We assume a dust scale height of $h_{\rm dust} = 0.10 \pm 0.02$ kpc, so that the extinction in the foreground of the lens is given by

$$A_{i,L} = \frac{1 - e^{-|D_L(\sin b)/h_{\rm dust}|}}{1 - e^{-|D_S(\sin b)/h_{\rm dust}|}} A_{i,S}, \tag{13}$$

where the index *i* refers to the passband: *I*, *V*, or *K*. In the Markov chain calculations themselves, we fix $D_S = 8.2$ kpc for our source star at a Galactic longitude of $l = 1.7647$, and we fix the dust scale height at $h_{\rm dust} = 0.10$ kpc. But we remove these restrictions by reweighting the links in the Markov chain when we sum them for our final results.

These five constraints have a very small effect on the overall χ^2. The addition of these constraints increases χ^2 by $\Delta\chi^2 = 1.41$, so it is clear that the light curve is quite consistent with these constraints.

While these constraints have almost no impact on the best-fit model χ^2, they have a dramatic effect on the allowed range of microlensing parallax parameters, as Figure 5 indicates. The 2σ range for $\pi_{E,N}$ is reduced from $-0.39 < \pi_{E,N} < 0.43$ to $0.18 < \pi_{E,N} < 0.25$, a reduction of a factor of 12 in uncertainty. This yields a microlensing parallax amplitude of $\pi_E = 0.265 \pm 0.02$, which will be used in Section 9 to determine the lens mass.

9. Lens Properties

For most planetary microlensing events, finite source effects provide a measurement of the source radius crossing time, t_*.

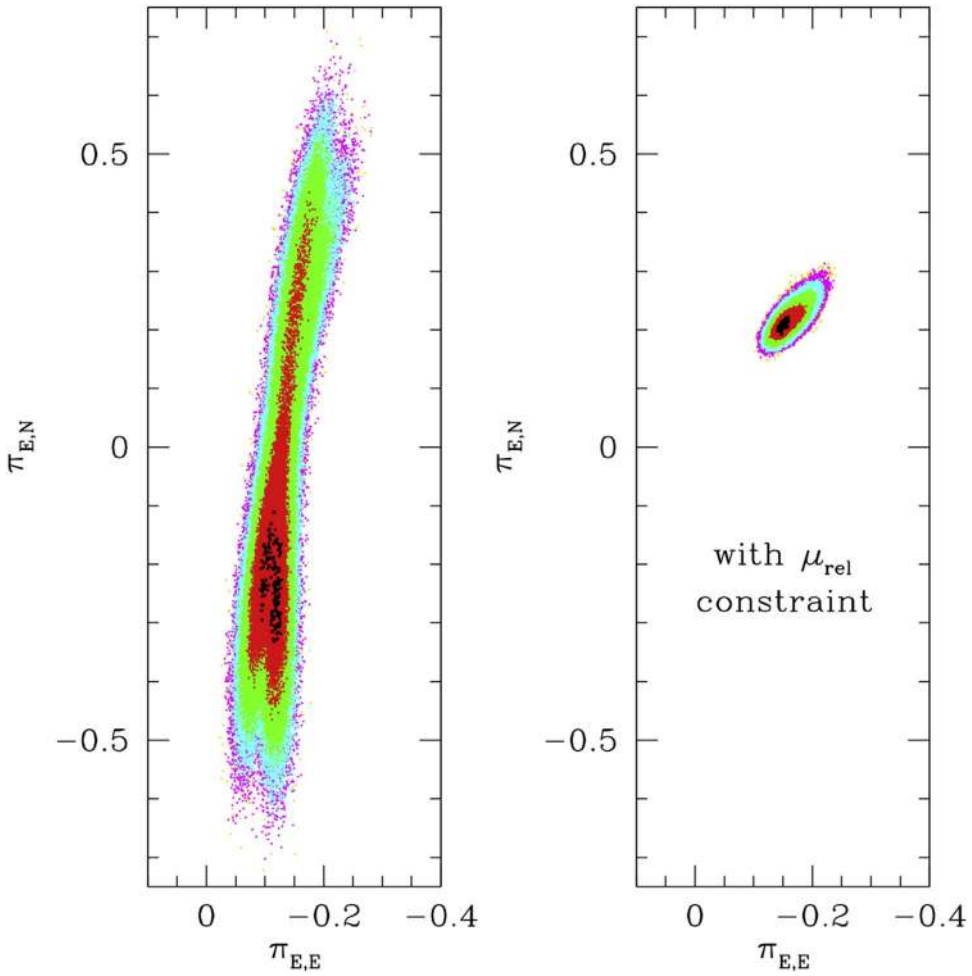

Figure 5. Left panel: $\boldsymbol{\pi}_{\rm E}$ distribution from light-curve modeling without any constraint from follow-up observations. Right panel: $\boldsymbol{\pi}_{\rm E}$ distribution resulting from the addition of the high-resolution follow-up imaging constraints. The following color scheme is used to denote the χ^2 differences from the best-fit light-curve model: black represents $\Delta\chi^2 < 1$, red represents $\Delta\chi^2 < 4$, green represents $\Delta\chi^2 < 16$, cyan represents $\Delta\chi^2 < 25$, and magenta represents $\Delta\chi^2 \geqslant 25$. The right panel clearly shows that the relative proper-motion measurements from *HST* and Keck constrain $\pi_{\rm E,N}$, which is the north component of $\boldsymbol{\pi}_{\rm E}$ that was largely unconstrained by the light curve. Without the $\boldsymbol{\mu}_{\rm rel,H}$ measurement, in the left panel, the light curve slightly favors solutions with $\pi_{\rm E,N} < 0$, but the constraint forces $\pi_{\rm E,N} > 0$. Note that this figure combines both the degenerate $u_0 > 0$ and $u_0 < 0$ models.

This allows the angular Einstein radius, θ_E, to be determined with the equation $\theta_E = \theta_* t_E / t_*$, where θ_* is the angular source radius, which can be determined by the source brightness and color (Kervella et al. 2004; Boyajian et al. 2014). However, t_* was not measured for OGLE-2012-BLG-0950, because this event did not reveal any finite source effects. Fortunately, it is also possible to determine θ_E from $\boldsymbol{\mu}_{\rm rel,G}$, which can be determined from the measured values of $\boldsymbol{\mu}_{\rm rel,H}$ and $\pi_{E,E}$ using Equations (11) and (12). The relation between the length of the $\boldsymbol{\mu}_{\rm rel,G}$ vector and θ_E is $\theta_E = t_E \mu_{\rm rel,G}$.

The measurement of either the angular Einstein radius, θ_E, or the microlensing parallax amplitude, π_E, will provide a mass–distance relation if we assume that the source distance, D_S, is known (Bennett 2008; Gaudi 2012):

$$M_L = \frac{c^2}{4G}\theta_E^2 \frac{D_S D_L}{D_S - D_L} = \frac{c^2}{4G}\frac{\rm au}{\pi_E^2}\frac{D_S - D_L}{D_S D_L}. \quad (14)$$

When both θ_E and π_E are known, the two mass–distance relations in Equation (14) can be multiplied together, yielding

$$M_L = \frac{c^2 \theta_E \,{\rm au}}{4G\pi_E} = \frac{\theta_E}{(8.1439\ {\rm mas})\,\pi_E} M_\odot, \quad (15)$$

which is a direct mass measurement with no dependence on D_L or D_S.

To solve for the planetary system parameters, we sum over our MCMC results using the Galactic model employed by Bennett et al. (2014) as a prior, weighted by the microlensing rate and the measured $\boldsymbol{\mu}_{\rm rel,H}$ value. The lens magnitude measurements were applied as constraints in the light-curve modeling, so we do not apply them again in the sum over the MCMC results. We do constrain the source distances to follow the microlensing rate weighted distribution according to our Galactic model, and we evaluate the extinction in the foreground of the lens using Equation (13) with the assumed error bar for $h_{\rm dust}$. The Galactic model is used to properly weight the source distances. However, using a fixed source distance of $D_S = 8.2$ kpc does not alter the results.

Figure 6 provides a graphical summary of the constraints on the host star in the mass–distance plane. The constraint from the one-dimensional microlensing parallax only is the magenta shaded region, while the red, black, and blue curves give the *K*-, *I*-, and *V*-band constraints from the Keck and *HST* follow-up observations, with 1σ error bars as dashed lines. Note that a single passband flux measurement combined with the one-dimensional parallax constraint yields a host star mass with

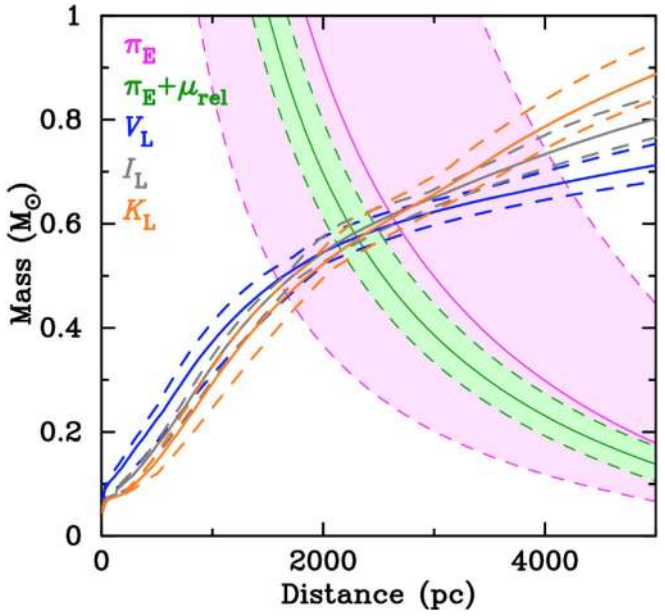

Figure 6. The mass–distance relation obtained from the microlensing parallax parameter determined by the light-curve models with the $\boldsymbol{\mu}_{\rm rel,H}$ constraint from the *HST* and Keck follow-up observations is plotted in green. The mass–distance relation from the light-curve model only, with no additional constraint on $\pi_{E,N}$, is shaded in magenta. The mass–distance relations obtained from the *K*-, *I*-, and *V*-band mass–luminosity relations with the lens flux constraints from Table 3 are plotted in red (Keck *K*), black (*HST I*), and blue (*HST V*). The solid lines are the best-fit values as a function of mass and distance. The dashed lines show the 1σ error bars. All three independent flux measurements in three different passbands result in the same solution. This confirms our identification of the lens star.

large uncertainty. The combination of lens flux constraints in three passbands does somewhat better, but it is the $\boldsymbol{\mu}_{\rm rel,H}$ measurement that gives the full $\boldsymbol{\pi}_{\rm E}$ determination indicated by the green shaded region. This is the critical feature that provides the precise determination of the host star mass, planet mass, and lens distance following the method described in Section 8. The host mass is measured to be $M_* = 0.58 \pm 0.04\,M_\odot$, an early-M or late-K dwarf star, orbited by a planet of twice Neptune's mass, $m_p = 39 \pm 8\,M_\oplus$, at a projected separation of $a_\perp = 2.54 \pm 0.23$ au. This also implies a lens system distance of $D_L = 2.19 \pm 0.23$ kpc. The fact that all three excess flux measurements give the same mass and distance indicates that there is no contamination of measurements from additional flux from another star (Bhattacharya et al. 2017; Koshimoto et al. 2017a).

We also use the lens flux and relative lens–source proper-motion measurements to constrain the light-curve models. The results of our final sum over the Markov chain light-curve models are given in Table 6 and Figure 7. The table gives the mean and rms uncertainty plus the central 95.4% confidence interval range for each parameter except the three-dimensional separation, $a_{\rm 3D}$, where we give the median and the central 68.3% confidence interval. The lens flux and parallax measurements exclude most of the masses and distances for this planetary system that were compatible with the light-curve model without any $\boldsymbol{\mu}_{\rm rel,H}$ or lens brightness constraints. These constraints also imply constraints on the parameters of the planetary system: the host star and planet mass and their separation and distance from Earth, as shown in Table 6. They are consistent with the parameters measured (shown in the previous paragraph) using the empirical mass–luminosity relations described in Section 8. Assuming a random orientation, this implies a three-dimensional separation of $a_{\rm 3d} = 3.0^{+1.7}_{-0.5}$ au. The uncertainties are the rms of the MCMC links.

10. Implications for *WFIRST*

This work is an important step in the development of the exoplanet mass-measurement methods (Bennett et al. 2007) for the *WFIRST* (Spergel et al. 2015) microlensing exoplanet survey (Bennett & Rhie 2002). This requires accurate relative astrometry of the blended source plus lens stars, just as we have done in this paper. In this analysis, we have measured the lens–source relative proper motion to a precision (in the *I* band) of 2%, despite the fact that the lens and source were separated by $\lesssim$0.5 FWHM. However, the situation is not directly analogous to *WFIRST*, because the *WFIRST* wide-field instrument has larger pixels (110 versus 40 mas) and observes mostly at longer wavelengths. Also, *WFIRST*'s prime mission will only allow a time baseline of 4 yr instead of the 5.78 yr elapsed between the OGLE-2012-BLG-0950 peak and the follow-up observations. On the other hand, the *WFIRST* detectors are $\gtrsim$5$\times$ more sensitive than the WFC3-UVIS detectors in the near-IR, and the dust extinction toward the bulge means that *WFIRST* will detect an order of magnitude or more photons per unit time than *HST* (Bennett & Rhie 2002; Penny et al. 2018).

Fortunately, Bennett et al. (2007) derived analytic estimates of the precision of these measurements that can be used to estimate the precision of the *WFIRST* mass measurements (Bennett et al. 2010a), so we can compare these analytic estimates to our measurements. These predictions only apply for images with a low background flux, so we will only compare to the *HST* analysis. Bennett et al. (2007) showed that, in most cases, fits with a constraint on the source flux are significantly more precise than unconstrained fits. However, a comparison between Tables 1 and 3 shows that the uncertainties in the source flux are about the same from the light-curve model and the unconstrained fit. So, we use Equation (8) of Bennett et al. (2007) because only the unconstrained fit analysis of that paper will apply. Using ePSF width measurements of 76 and 72 mas for the F814W and F555W passbands, respectively, we find predicted lens–source separation measurement precisions of 1.3 and 2.3 mas for the F814W and F555W bands. These measured precisions in Table 4 are 0.7 and 1.3 times the predictions from Bennett et al. (2007)'s Equation (8) for the F814W and F555W bands, respectively. The fact that we can do better than Bennett et al. (2007) is likely due to the fact that the Bennett et al. (2007) results are based on only the lowest-order terms in the separation over the FWHM.

The *HST* observations of MOA-2008-BLG-310 (Bhattacharya et al. 2017) provide a test case with much lower S/N. The star blended with the source for this event is not the lens, but it is very likely that the lens is >3.5 mag fainter than the blended star (assuming that massive stars are not much more likely to host a planet of $q = 3.3 \times 10^{-4}$). So, the source flux constrained fits from Bhattacharya et al. (2017) should be a good test of the source flux constrained formula (Equation (4)) from this paper. From the 2014 *HST* observations of this event, Bhattacharya et al. (2017) measured consistent lens-blend separations of 14.1 ± 2.1 mas in the *I* band and 13.5 ± 2.4 mas in the *V* band, which compare to predicted uncertainties of 1.5 and 1.0 mas in the F814W and F555W bands, respectively. So, the observed uncertainties are only 1.4$\times$ larger than the prediction for the F814W band but

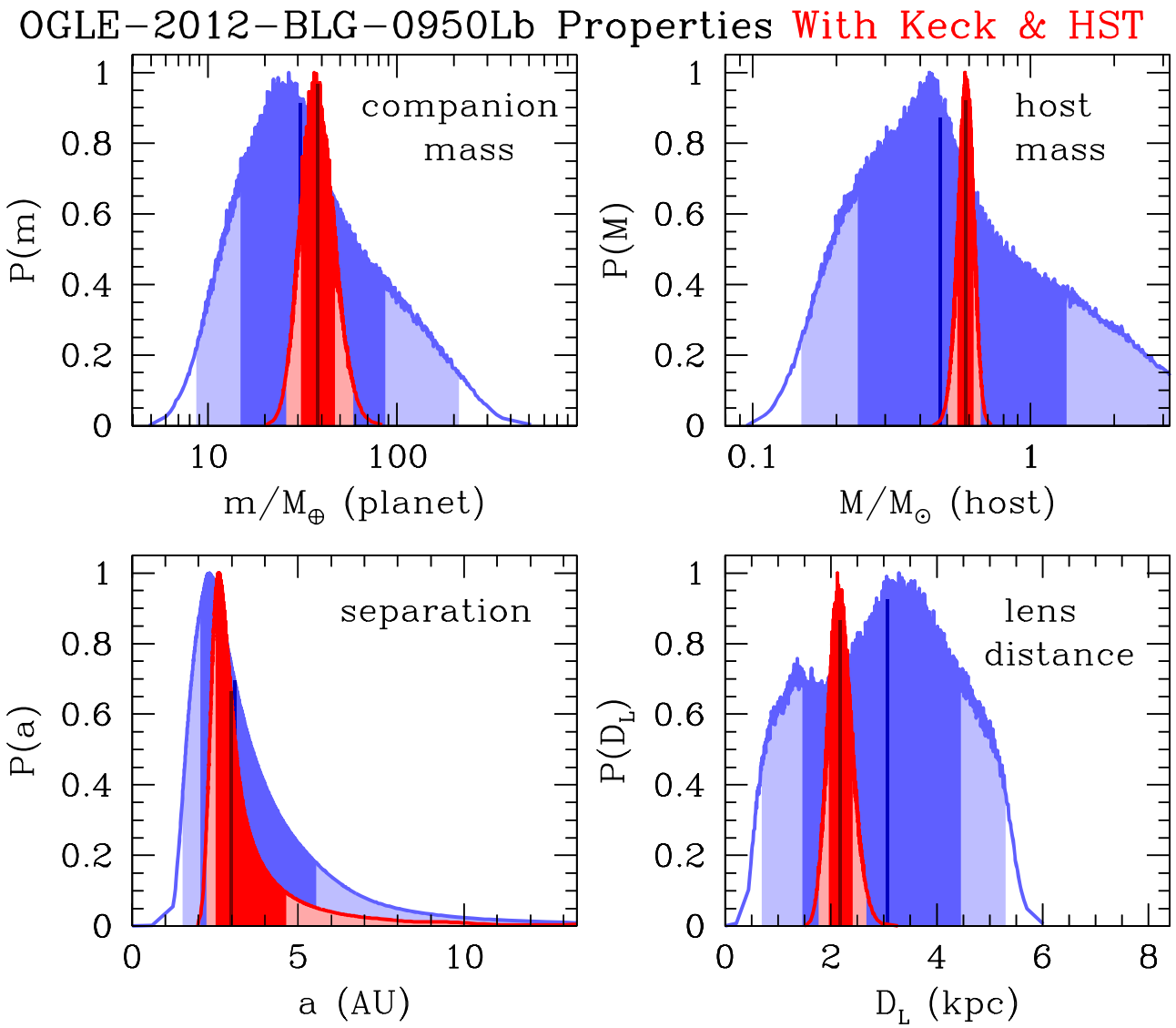

Figure 7. The Bayesian posterior probability distributions for the planetary companion and host mass, their separation, and the distance to the lens system are shown with only light-curve constraints in blue and additional constraints from our Keck and *HST* follow-up observations in red. The central 68.3% of the distributions are shaded in darker colors (dark red and dark blue), and the remaining central 95.4% of the distributions are shaded in lighter colors. The vertical black line marks the median of the probability distribution of the respective parameters.

Table 6
Measurement of Planetary System Parameters from the Lens Flux Constraints

Parameter	Units	Values and rms	2σ Range
Angular Einstein radius, θ_E	mas	1.26 ± 0.08	1.10–1.14
Geocentric lens–source relative proper motion, $\mu_{\rm rel,G}$	mas yr^{-1}	6.74 ± 0.42	5.92–7.58
Host star mass, M_*	$M_\odot$	0.58 ± 0.04	0.51–0.67
Planet mass, m_p	$M_\oplus$	39 ± 8	26–59
Host star–planet 2D separation, $a_\perp$	au	2.54 ± 0.23	2.13–3.03
Host star–planet 3D separation, $a_{\rm 3D}$	au	$3.0^{+1.7}_{-0.5}$	2.2–10.8
Lens distance, D_L	kpc	2.19 ± 0.23	1.77–2.68

2.4× larger for the F555W band. The *I*-band results are encouraging, but we suspect that the lower precision in the *V* band may be because the eight dithered images are not sufficient to model the ePSF in the more severely undersampled *V* band. We hope to investigate this issue with F555W observations with more dither positions.

The *WFIRST* high angular resolution observations differ from our high angular resolution *HST* observations in several respects. The *WFIRST* (Spergel et al. 2015; Penny et al. 2018) operates in the IR with detectors that are much more sensitive than the *HST* WFC3-UVIS detectors are in the F814W passband, and *WFIRST* will have many more observations in

each observing season than we can obtain with *HST*. The *WFIRST* will have ∼800× more observations in its wide W149 passband and ∼20× more observations in the Z087 passband. On the other hand, *WFIRST* observations taken with the same telescope orientation in the prime mission will be no more than 4 yr apart, and *WFIRST*'s wide-field instrument pixels subtend 110 mas, 2.75 larger than the *HST*-WFC3 pixels. So, *WFIRST* collects many more photons, but it will observe the lens and source stars at separations that are typically smaller than the separations of the lens and source stars in our *HST* and Keck follow-up program. For a specific example, let us consider a system just like OGLE-2012-BLG-0950 but with source and lens magnitudes that are 2 mag fainter. If we consider observations of their separation 4 yr after the event, when the lens–source separation is 23.5 mas, Equation (8) of Bennett et al. (2007) gives a separation uncertainty of 2.6 mas, or 11%, based on 144 observations in the Z087 passband. This assumes an effective FWHM of 131 mas, including a *WFIRST* model PSF and pixelization effects. However, *WFIRST* will provide tighter constraints on the source flux, so we can also use Bennett et al. (2007)'s Equation (4) with the source flux constraint. This gives a much tighter limit on the lens–source separation, so we consider observations 3 yr after the event, instead of 4 yr. With this constrained fit, we obtain a predicted lens–source separation uncertainty of 0.43 mas, which is 2.4% of the 17.6 mas separation after 3 yr. With ∼50× as many observations and >5× as many photons, the ultrawide W149 passband may obtain much higher S/N than Z087, but the color dependence of the PSFs with such a wide passband is a complication. Fortunately, the Z087 observations seem sufficient to make these measurements for most of our events.

11. Discussion and Conclusions

With near-simultaneous high angular resolution follow-up observations from Keck and *HST*, we have measured the angular separation of the source and planetary host star to be 34 mas in three different passbands, *K*, *I*, and *V*. This separation measurement allows us to convert the partial measurement of the microlensing parallax from the light curve into a complete measurement of the two-dimensional $\boldsymbol{\pi}_{\rm E}$ vector. The combination of this microlensing parallax measurement and the θ_E value determined from the measured lens–source separation determines the lens mass and distance. This lens mass and distance provides lens magnitude predictions that are confirmed independently in three different passbands. This rules out alternative explanations of this event involving additional stars, such as a companion to the lens or source. The one highly unlikely possibility that is not yet excluded is that the detected excess flux could come from an $\sim 0.6\,M_\odot$ companion to a white dwarf planetary host star that is also $\sim 0.6\,M_\odot$. According a statistical study by Holberg et al. (2013), the probability of a white dwarf hosting a main-sequence companion is ∼8%, but the vast majority of these white dwarf–main-sequence star binaries have separations that are much too large for the main-sequence star to be confused with the lens. So, the fraction of white dwarfs with binary companions that could be confused with the lens star is about 1%. However, it is not guaranteed that a binary companion to a white dwarf lens would have *V*-, *I*-, and *K*-band magnitudes compatible with the lens mass inferred from the $\pi_{\rm E,E}$ measurement and the apparent $\boldsymbol{\mu}_{\rm rel,H}$ measurement, so the probability that a white dwarf host with a binary companion could produce the light curve and follow-up data for this event is $\lesssim$0.1%. To avoid a light-curve signal from this binary companion, this companion would need to be separated by $\gtrsim 10\theta_E \approx 13$ mas from the lens at the time of the event. This means that this unlikely possibility of a white dwarf host star with a main-sequence companion could be tested with an additional epoch of follow-up observations to confirm that the relative proper motion of the main-sequence star does extrapolate back to the position of the source at the time of the event, as we have shown for planetary microlensing event OGLE-2005-BLG-169 (Batista et al. 2015; Bennett et al. 2015).

The measured planetary mass of $m_p = 39 \pm 8\,M_\oplus$ is of particular interest because the core accretion theory predicts that such planets should be rare. The core accretion theory includes a runaway gas accretion phase (Pollack et al. 1996; Lissauer et al. 2009) that is thought to imply that planets in the mass range 20–80 $M_\oplus$ are rare. According to this theory, beyond the snow line, a planetary core rapidly grows by the accumulation of planetesimals until it reaches a mass of $\sim 10\,M_\oplus$ (Pollack et al. 1996; Rafikov 2011). Further growth is dominated by gas accretion that starts slowly, but when the gas mass grows to equal the core mass, growth is thought to become a runaway exponential process. This process is thought to continue very rapidly until it is terminated by a lack of gas at a mass similar to that of Jupiter ($318\,M_\oplus$) or possibly Saturn ($95\,M_\oplus$).

The cold exoplanet mass ratio function measured by Suzuki et al. (2016) finds no evidence for a dearth of planets at these intermediate, 20–80 $M_\oplus$, masses. The measured mass ratio function increases smoothly from a mass ratio of $q = 0.03$ down to a mass ratio of $q \approx 10^{-4}$, where it reaches a peak (Udalski et al. 2018). There is no evidence of a mass ratio gap at $(1\text{–}4) \times 10^{-4}$, where we would expect to see this expected low occurrence rate of 20–80 $M_\oplus$ mass planets. However, since Suzuki et al. (2016) considered only mass ratios and not masses, it remains possible that a gap in the exoplanet mass distribution is smoothed out by the combination of a range of host stars from very low mass stars up to solar-type stars. Perhaps planet formation is different for very low mass stars in a way that smooths out the gap in the exoplanet mass distribution around solar-type stars.

Our follow-up high angular resolution imaging program addresses this issue directly by determining the masses of the microlens host stars and their planets. The planet OGLE-2012-BLG-0950Lb is the first planet from the Suzuki et al. (2016) sample to have a mass measured to be in the 20–80 $M_\oplus$ range, but our ongoing follow-up observing program will measure masses of more host stars and planets from the Suzuki et al. (2016) sample to provide a more definitive answer to this question. Our program has also identified a similar-mass planet, OGLE-2012-BLG-0026Lb (Beaulieu et al. 2016), with a mass of $46.0 \pm 2.5\,M_\oplus$, orbiting a solar-type star. This planet is one of two planets detected in this microlensing event that is, unfortunately, not part of the Suzuki et al. (2016) sample.

This analysis has also been the first example of a full microlensing parallax measurement being obtained from light-curve measurement of one component of the $\boldsymbol{\pi}_{\rm E}$ vector and a follow-up measurement of the heliocentric lens–source relative proper motion, $\boldsymbol{\mu}_{\rm rel,H}$. This is also an important part of the *WFIRST* exoplanet mass-measurement tool set (Bennett et al. 2007), and in most cases, it will allow for mass measurements that are independent of the flux detected from the host star. The

flux of the lens is also measured in three passbands, giving rise to additional redundant consistent constraints on the host star and planet masses and distance. The lens and source are not separately resolved in any of the images, but still we measure the separation at a high significance. This combination of the unresolved lens–source separation measurement and flux measurement in multiple passbands plus the one-dimensional parallax measurement includes all the major *WFIRST* mass-measurement methods, as discussed in Bennett et al. (2007) and Yee (2015).

We acknowledge the help of Dr. Peter Stetson in operating DAOPHOT and providing us with a current version of the code and feedback on our analysis of Keck data. This paper is based in part on observations made with the NASA/ESA *Hubble Space Telescope*, which is operated by the Association of Universities for Research in Astronomy, Inc., under NASA contract NAS 5-26555. These observations are associated with program GO-15455. The Keck Telescope observations and analysis were supported by a NASA Keck PI Data Award, administered by the NASA Exoplanet Science Institute. Data presented herein were obtained at the W. M. Keck Observatory from telescope time allocated to the National Aeronautics and Space Administration through the agency's scientific partnership with the California Institute of Technology and the University of California. The Observatory was made possible by the generous financial support of the W. M. Keck Foundation. DPB, AB, and CR were also supported by NASA through grant NASA-80NSSC18K0274. A.U. was supported by the OGLE project funded by National ScienceCentre, Poland with the grant MAESTRO 2014/14/A/ST9/00121.

ORCID iDs

J.-P. Beaulieu https://orcid.org/0000-0003-0014-3354
D. P. Bennett https://orcid.org/0000-0001-8043-8413
N. Koshimoto https://orcid.org/0000-0003-2302-9562
J. R. Lu https://orcid.org/0000-0001-9611-0009
A. Fukui https://orcid.org/0000-0002-4909-5763
P. Mroz https://orcid.org/0000-0001-7016-1692
C. Ranc https://orcid.org/0000-0003-2388-4534

References

Alcock, C., Allsman, R. A., Alves, D. R., et al. 2001, Natur, 414, 617
Anderson, J., & Bedin, L. R. 2010, PASP, 122, 1035
Anderson, J., & King, I. R. 2000, PASP, 112, 1360
Anderson, J., & King, I. R. 2004, Hubble Space Telescope Advanced Camera for Surveys Instrument Science Report 04-15
Anderson, J., & King, I. R. 2006, Hubble Space Telescope Advanced Camera for Surveys Instrument Science Report 2006-11
Batista, V., Beaulieu, J.-P., Bennett, D. P., et al. 2015, ApJ, 808, 170
Batista, V., Beaulieu, J.-P., Gould, A., et al. 2014, ApJ, 780, 54
Beaulieu, J. P., Batista, V., Bennett, D. P., et al. 2018, AJ, 155, 78
Beaulieu, J. P., Bennett, D. P., Batista, V., et al. 2016, ApJ, 824, 2
Bennett, D. P. 2008, in Exoplanets, ed. J. Mason (Berlin: Springer) arXiv:0902.1761
Bennett, D. P. 2010, ApJ, 716, 1408
Bennett, D. P., Anderson, J., Beaulieu, J.-P., et al. 2010a, arXiv:1012.4486
Bennett, D. P., Anderson, J., Bond, I. A., Udalski, A., & Gould, A. 2006, ApJL, 647, L171
Bennett, D. P., Anderson, J., & Gaudi, B. S. 2007, ApJ, 660, 781
Bennett, D. P., Batista, V., Bond, I. A., et al. 2014, ApJ, 785, 155
Bennett, D. P., Bhattacharya, A., Anderson, J., et al. 2015, ApJ, 808, 169
Bennett, D. P., Rhie, S., Nikolaev, S., et al. 2010b, ApJ, 713, 837
Bennett, D. P., & Rhie, S. H. 1996, ApJ, 472, 660
Bennett, D. P., & Rhie, S. H. 2002, ApJ, 574, 985
Bennett, D. P., Rhie, S. H., Udalski, A., et al. 2016, AJ, 152, 125
Bennett, D. P., Sumi, T., Bond, I. A., et al. 2012, ApJ, 757, 119
Bennett, D. P., Udalski, A., Bond, I. A., et al. 2018, arXiv:1806.06106
Bertin, E., & Arnouts, S. 1996, A&AS, 117, 393
Bertin, E., Mellier, Y., Radovich, M., et al. 2002, in ASP Conf. Ser. 281, Astronomical Data Analysis Software and Systems XI, ed. D. A. Bohlender, D. Durand, & T. H. Handley (San Francisco, CA: ASP), 228
Bhattacharya, A., Bennett, D. P., Anderson, J., et al. 2017, AJ, 154, 59
Bond, I. A., Bennett, D. P., Sumi, T., et al. 2017, MNRAS, 469, 2434
Boyajian, T. S., van Belle, G., & von Braun, K. 2014, AJ, 147, 47
Cardelli, J. A., Clayton, G. C., & Mathis, J. A. 1989, ApJ, 345, 245C
Carpenter, J. M. 2001, AJ, 121, 2851
Cousins, A. W. J. 1976, MmRAS, 81, 25
Delfosse, X., Forveille, T., Ségransan, D., et al. 2000, A&A, 364, 217
Dong, S., Bond, I. A., Gould, A., et al. 2009, ApJ, 698, 1826
Gaudi, B. S. 2012, ARA&A, 50, 411
Gaudi, B. S., Bennett, D. P., Udalski, A., et al. 2008, Sci, 319, 927
Gehrels, N. 2010, arXiv:1008.4936
Ghosh, H., DePoy, D. L., Gal-Yam, A., et al. 2004, ApJ, 615, 450
Gould, A. 2014, JKAS, 47, 215
Gould, A., Bennett, D. P., & Alves, D. R. 2004, ApJ, 614, 404
Gould, A., & Loeb, A. 1992, ApJ, 396, 104G
Gubler, J., & Tytler, D. 1998, PASP, 110, 738
Henry, T. J., Franz, O. G., Wasserman, L. H., et al. 1999, ApJ, 512, 864
Henry, T. J., & McCarthy, D. W., Jr. 1993, AJ, 106, 773
Holberg, J. B., Oswalt, T. D., Sion, M. A., Barstow, A., & Burleigh, M. R. 2013, MNRAS, 435, 2077
Janczak, J., Fukui, A., Dong, S., et al. 2010, ApJ, 711, 731
Johnson, H. L. 1966, ARA&A, 4, 193
Kenyon, S. J., & Hartmann, L. 1995, ApJSS, 101, 117
Kervella, P., Thévenin, F., Di Folco, E., & Ségransan, D. 2004, A&A, 426, 297
King, I. R. 1983, PASP, 95, 163K
Koshimoto, N., Shvartzvald, Y., Bennett, D. P., et al. 2017a, AJ, 154, 3
Koshimoto, N., Udalski, A., Beaulieu, J. P., et al. 2017b, AJ, 153, 1
Kozhurina-Platais, V. 2012, STScI Instrument Science Report WFC 2014-12
Kozlowski, S., Wozniak, P. R., Mao, S., & Wood, A. 2007, ApJ, 671, 420
Kubas, D., Beaulieu, J. P., Bennett, D. P., et al. 2012, A&A, 540, A78
Lauer, T. R. 1999, PASP, 111, 227
Lissauer, J. J., Hubickyj, O., D'Angelo, G., & Bodenheimer, P. 2009, Icar, 199, 338
Lu, J. R., Neichel, B., Anderson, J., et al. 2014, Proc. SPIE, 9148, 91480B
Minniti, D., Lucas, P. W., Emerson, J. P., et al. 2010, NewA, 15, 433
Muraki, Y., Han, C., Bennett, D. P., et al. 2011, ApJ, 741, 22
Penny, M. T., Gaudi, B. S., Kerins, E., et al. 2018, arXiv:1808.02490
Pollack, J. B., Hubickyj, O., Bodenheimer, P., et al. 1996, Icar, 124, 62
Rafikov, R. R. 2011, ApJ, 727, 86
Service, M., Lu, J. R., Campbell, R., et al. 2016, PASP, 128, 095004
Spergel, D., Gehrels, N., Baltay, C., et al. 2015, arXiv:1503.03757
Stern, D., Bartlett, J. G., Brodwin, M., et al. 2010, arXiv:1008.3563
Stetson, P. B. 1987, PASP, 99, 191S
Sumi, T., Udalski, A., Bennett, D. P., et al. 2016, ApJ, 825, 112
Suzuki, D., Bennett, D. P., Sumi, T., et al. 2016, ApJ, 833, 145
Szymański, M. K., Udalski, A., Soszyński, I., et al. 2011, AcA, 61, 83
Udalski, A., Ryu, Y.-H., Sajadian, S., et al. 2018, AcA, 68, 1
Verde, L., Reiris, H. V., & Spergel, D. N. 2003, ApJS, 148, 195
Yee, J. C. 2015, ApJL, 814, L11
Yelda, S., Lu, J. R., Ghez, A. M., et al. 2010, ApJ, 725, 331